RESEARCH PAPER



Numerical investigation of laser powder bed fusion of glass

Kyriaki Corinna Datsiou 🕒 · Ian Ashcroft

Received: 4 March 2024 / Accepted: 6 June 2024 / Published online: 2 July 2024 © The Author(s) 2024

Abstract Additive manufacturing of glass using laser powder bed fusion has been recently developed, demonstrating its potential to be applied in small scale applications such as flow reactors for the chemical engineering and pharmaceutical manufacturing industries. While previous research demonstrated that complex 3dimensional shapes can be manufactured, built parts are often brittle, exhibit high porosity and lack transparency. This study employs a transient, heat transfer finite element analysis to shed light on the thermal response of laser—glass powder bed interaction and the impact of processing parameters. Through this understanding, the research seeks to identify practical strategies that can be employed to improve the quality and properties of the built parts. Bulk solid and powder soda lime silica glass properties are used as input in the model, while the laser heat flux and scan strategy, conversion of powder feedstock to bulk solid glass and heat losses from convection and radiation effects are introduced in the model through Fortran coding. The study showed that effective powder consolidation, resulting in well-defined geometrical features, is achieved for temperatures near the glass melting point. Additionally, uniform consolidation depths and widths can be achieved by increasing laser power, elevating substrate temperature and reducing scan speed within certain limits, whilst ensuring hatch spacing is below the corresponding single scan track width for unidirectional adjacent laser trajectories.

Keywords Glass · Additive manufacturing · Laser powder bed fusion · Finite element analysis · Heat transfer analysis

1 Introduction

Additive manufacturing, has emerged as a pivotal technology in recent decades, facilitating the manufacture of complex geometries with minimal waste. It offers substantial benefit in customising components to meet specific requirements while being cost-effective for prototyping or where a limited number of components is required. The above apply to metals, ceramics and polymers and could also extend to glass. While it is acknowledged that additive manufacturing of glass cannot currently outperform the efficiency of traditional manufacturing methods, such as the wellestablished float process for flat glass or moulding and extrusion processes for mass production components, it offers significant advantage for developing complex geometries that are challenging or impractical to achieve through conventional means.

K. C. Datsiou (⋈)

Centre for Engineering Research, School of Physics, Engineering and Computer Science, University of Hertfordshire, Hatfield, UK e-mail: kd21abe@herts.ac.uk

I. Ashcroft

Centre for Additive Manufacturing, University of Nottingham, Nottingham, UK e-mail: ian.ashcroft@nottingham.ac.uk



Additive manufacturing for glass to date spans across direct and indirect methods (Xin et al. 2023). Direct methods involve high temperatures to sinter/melt glass feedstock in a single step process such as laser powder bed fusion (Datsiou et al. 2019, 2021; Fateri & Gebhardt 2015), extrusion (Inamura et al. 2018; Klein 2015) and directed energy deposition (Grabe et al. 2021; Spirrett et al. 2023). In contrast, indirect methods are performed at ambient conditions using a composite material, i.e. a binder that encapsulates the glass feedstock, to print a "green" part. This is followed by post-processing, that may include drying, binder burning and sintering steps. Stereolithography (Kotz et al. 2017; Liu et al. 2018) and direct ink writing (Nguyen et al. 2017) are notable for glass among indirect methods. Although indirect methods are recognised for their ability to produce optically transparent parts, these often lack in dimensional accuracy due to anisotropic shrinkage associated with post processing. Laser powder bed fusion has the potential to address this limitation as a single step process. Moreover, it presents the additional advantage of preventing "layered" features and anisotropic properties, that are commonly associated with nozzle-based processes such as extrusion.

To date, process maps for laser powder bed fusion (LPBF) of soda lime silica glass have been populated to identify its processing window (Datsiou et al. 2019, 2021). These studies also demonstrated the ability to manufacture complex 3-dimensional shapes, such as the lattice structures illustrated in Fig. 1. However, glass remains a challenging material to process with LPBF. Its low absorptivity for wavelengths used in most LPBF systems (typically operating around 1100 nm) impedes laser processing. Coupled with the high melting temperature of glass, this leads to high energy density requirements for achieving feedstock consolidation. Consequently, the LPBF process generates high temperature gradients within the built parts leading to the development of thermal stress and cracking, which affects the flexural strength (Datsiou et al. 2021) and thereby limits the application of this technology.

Finite Element Analysis (FEA) has emerged as a fundamental tool for better understanding the thermal behaviour of the LPBF process in metals. Despite numerical challenges in realistic modelling of the laser source, providing accurate material properties and realistic accounting for heat losses, experimental thermal investigation is difficult to undertake due to localised



Fig. 1 Additively manufactured lattice structures of soda lime silica glass with laser powder bed fusion (Datsiou et al. 2021)

ultra-fast heating—cooling and melting—solidification phenomena. Early studies employed numerical models to simulate the thermal behaviour and predict temperature distributions and melt pool characteristics during LPBF (Gusarov & Smurov 2010; Kolossov et al. 2004; Roberts et al. 2009). More recently FEA was used for optimisation, providing the correlation between thermal response and laser processing parameters (Li et al. 2020; Li & Gu 2014; Zhang et al. 2018) while thermomechanical analyses were also used to predict residual stress development and optimise scan strategies (Parry et al. 2016; Wu et al. 2017).

Despite the available research on the numerical optimisation of LPBF for metals, there is a lack of research on glass. This study develops a transient, heat transfer finite element analysis model of a moving heat source operating in a glass powder bed in order to capture the thermal behaviour and investigate consolidation characteristics. The model is validated against experimental results and is subsequently extended to capture the impact of set-up and processing parameters, including substrate material and preheating temperature, laser power, scan speed and hatch spacing. The primary goal of this study is to gain a comprehensive understanding of the thermal response of LPBF of glass and identify practical strategies that can be employed to improve the quality of built parts. Section 2 below provides an overview of the method, including a detailed description of the FEA model and the material properties of glass. Section 3 presents and discusses the obtained results, including the validation of the numerical model against experimental results, whilst Section 4 summarises important results and conclusions.



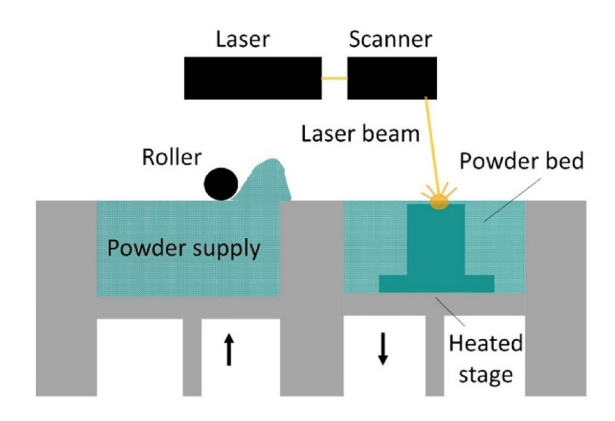


Fig. 2 Laser powder bed fusion

2 Method

LPBF is an iterative additive manufacturing process extensively used for metals. In LPBF, a high-power laser is used to selectively sinter or melt powder particles in layers of controlled thickness to create a three-dimensional object (Fig. 2). In detail, a thin layer of powder is spread on the build platform for processing, which incorporates a heated stage to reduce temperature gradients and hence, residual stress in built parts. The layer is subsequently processed by the laser source which moves in predetermined trajectories based on the selected scan strategy and the cross section of the geometrical model. After each layer is processed, the stage moves downwards, and a fresh layer of powder is deposited. The sequence is repeated until the built part is complete.

In this study a thermal FEA model is developed to simulate the LPBF process and predict the heat distribution within the powder bed. Heat conduction in solids takes the following form:

$$Q = \rho C_p \frac{\partial T}{\partial t} - \nabla \cdot (\lambda \nabla T) \tag{1}$$

where Q is the volumetric heat flux, ρ is the density of the material, C_p is the specific heat capacity, λ is the thermal conductivity and T is the temperature.

This can be expressed in 3d coordinate space as follows:

$$\rho C_p \frac{\partial T}{\partial t} = \frac{\partial}{\partial x} \left(\lambda \frac{\partial T}{\partial x} \right) + \frac{\partial}{\partial y} \left(\lambda \frac{\partial T}{\partial y} \right) + \frac{\partial}{\partial z} \left(\lambda \frac{\partial T}{\partial z} \right) + Q$$
(2)

In addition to conduction, heat losses q_{tot} (Eq. 4), arising from convection q_{con} , and radiation q_{rad} , effects (Eq. 3a-b) also occur and must be considered in the analysis.

$$q_{con} = h_c(T - T_0) \tag{3a}$$

$$q_{rad} = \varepsilon_p \sigma \left(T^4 - T_0^4 \right) \tag{3b}$$

$$q_{tot} = h_c + \varepsilon_p \sigma (T + T_0) \left(T^2 - T_0^2 \right) \tag{4}$$

where $h_{\rm c}$ is the heat transfer coefficient, $\varepsilon_{\rm p}$ is the emissivity of the powder bed, $\sigma = 5.67 \cdot 10^{-8} \ {\rm W/m^2 K^4}$ is the Stefan Boltzmann constant and T_0 is the temperature of the environment.

2.1 Finite element analysis model

The FEA model was developed in Abagus 2023 (Dassault Systemes, USA) to simulate the laser powder bed fusion process through a transient heat transfer analysis. The model closely matches the set-up used in the experimental studies of Datsiou et al., (2019, 2021). In detail, the model (Fig. 3) features a 1.5 \times 1.5 \times 0.07 mm^3 glass powder bed on a $2.0 \times 2.0 \times 0.5 \text{mm}^3$ dense substrate. Alumina substrates were considered in this study unless otherwise specified. The model was discretised with 8-node, full integration heat transfer brick elements, DC3D8, (Abagus 2023 Documentation 2023). A fine mesh with an element size of 30 μm was used for the powder bed with a total of 22,405 elements. while a coarser mesh was used for the alumina substrate to reduce the computational cost. A mesh convergence study with varying density for the mesh (Fig. 4) was initially undertaken for a single linear scan track (laser power P = 75 W and scan speed v = 26 mm/s) confirming the suitability of the selected mesh (22,405 elements) and providing balance between output accuracy and computational cost.

Individual analysis steps were introduced in the FEA model to describe each step of the LPBF process for a single layer i.e. pre-heating of the substrate and laser processing of the powder bed.

Preheating of the substrate: A step with a time period of 1 s was introduced at the beginning of the analysis. This time period was found to be sufficient for the substrate to be effectively pre-heated. A fixed temperature



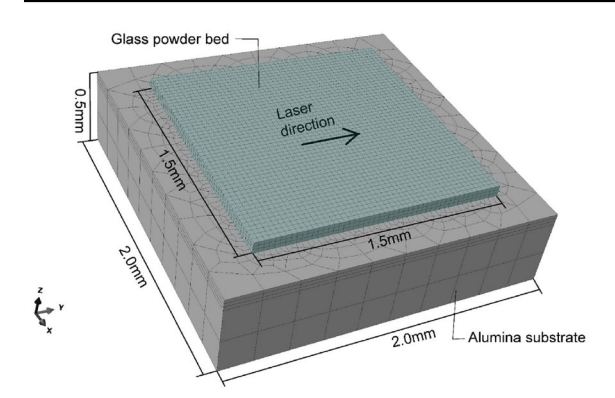


Fig. 3 FEA model

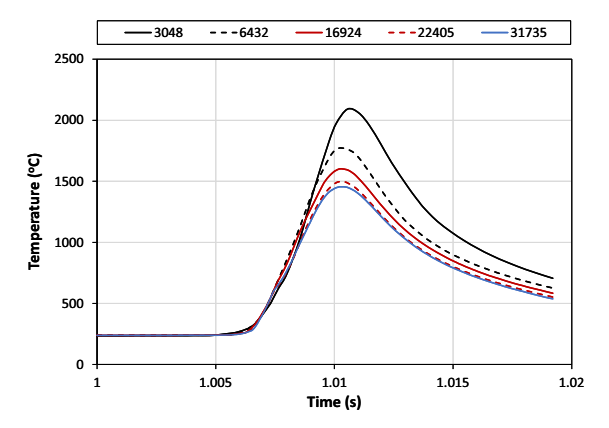


Fig. 4 Temperature output during laser processing for powder bed models of 3,048 to 31,735 elements for laser power of P =75 W and scan speed of v = 26 mm/s

of 250 °C (unless otherwise specified) was applied to the lower and side surfaces of the substrate. This was to replicate the experimental conditions in which these surfaces are in direct contact with the heat source. The pre-heating temperature was preserved during the process while an ambient temperature of 20 °C was used.

Laser processing of the powder bed: A laser processing step was introduced after the preheating step. Its time period was adjusted to account for the selected laser scan speed and the scan strategy / distance to be covered. Laser processing of the powder bed was incorporated through a moving heat flux, described by a Gaussian distribution (Papazoglou et al. 2022) which

$$q = \frac{2\eta P}{\pi R_0^2} exp\left(-\frac{2r^2}{R_0^2}\right)$$
 (5)

takes the following form:

where η is the absorption coefficient for the powder, P is the laser power, R_0 is the laser spot size and r is the radial distance from the centre of the laser beam to the point of interest on the powder bed.

The heat flux input was defined in a DFLUX usersubroutine through a Fortran script. The scan strategy (laser trajectories) and the laser processing parameters including laser power, scan speed and spot size were also included in the script.

Powder consolidation was integrated in the FEA model through a solution dependent state variable (SDV). During the analysis the state variable changed as a function of temperature based on the output results. A state variable value of:

- \bullet SDV = 0 was used to describe glass powder elements. This was the opening value assigned to all elements of each new powder layer by default. Powder elements that did not consolidate during laser processing maintained SDV = 0.
- SDV = 1 described bulk solid glass elements that consolidated during the process. The SDV changed from 0 to 1 when the element temperature exceeded the transition temperature of glass ($T_g = 575$ °C). For $T \ge T_g$, powder particles soften and fuse together beyond the transition temperature, leading to powder consolidation, without necessarily reaching the melting temperature of glass ($T_{\rm m} = 1280$ °C), (Kamyabi et al. 2017).

The phase change from powder to solid was implemented in Abagus with a USDFLD user-subroutine, coded in Fortran. The solution dependent state variable was updated in every analysis increment and determined the material properties (glass powder or bulk solid glass) to be used per element.

Heat losses from convection and radiation effects were combined as shown in Eq. 4 and considered in all steps of the analysis through a FILM user subroutine, that was also coded in Fortran. A summary of relevant input parameters used for the FEA model are available in Table 1.

Overall, a total of 23 FEA models of the LPBF process of a single layer were undertaken in this study to understand the thermal behaviour and the consolidation characteristics for soda lime silica glass. The investigation involved a parametric study of the effects of laser power, scan speed, hatch spacing and substrate temperature and material to explore their impact on the additive manufacturing process.



Table 1 Summary of FEA input parameters

Property	Variable	Value	Comments/Reference
Laser wavelength	λ_{w} (nm)	1064	ReaLizer GmbH SLM-50, Germany
Laser Spot size	R_0 (µm)	60	for a focus position of 9.55 mm, (Batalha et al. 2020; Datsiou et al. 2021)
Substrate temperature	T_{sub} (°C)	250*	(Datsiou et al. 2019, 2021)
Layer Thickness	$t_1 (\mu \mathrm{m})$	70*	(Datsiou et al. 2019, 2021)
Laser power	P(W)	$20 \le P \le 120$	
Scan speed	v (mm/s)	$10 \le v \le 60$	
Convection coefficient	$h_{\rm c}~({ m W/m^2K})$	14.73	For argon gas in Realizer GmbH SLM-50 (B. Liu 2013)

^{*}Unless otherwise specified

2.2 Materials

The powder feedstock material used in this study was soda lime silica glass (72.1% SiO2—13.7% Na2O—10.2% CaO—2.5% MgO—1.1% Al2O3) with an average particle size of 44 μ m, to match the feedstock material used in Datsiou et al., (2021). The material properties for the FEA model were defined for both glass powder (SDV = 0) and bulk solid (SDV = 1) states. The thermal conductivity, λ_s , and specific heat capacity, $C_{\rm p,s}$, for bulk solid glass are temperature dependent and respectively described by Eqs. 6 and 7 (Carré & Daudeville 1999):

$$\lambda_s = 0.975 + 0.000858T \tag{6}$$

$$C_{p,s} = 893 + 0.4T - \frac{1.8 \cdot 10^{-7}}{T^2} \tag{7}$$

where T is the material temperature in $^{\circ}$ C.

The Sih & Barlow (1992) model was subsequently employed to predict the effective thermal conductivity of the powder bed, which is simplified to the following form based on Dai & Shaw, (2004):

$$\frac{\lambda_{eff}}{\lambda_{f}} = \left(1 - \sqrt{1 - \varphi}\right) \left(1 + \frac{\varphi \lambda_{r}}{\lambda_{f}}\right) + \left(\sqrt{1 - \varphi}\right) \\
\left(\frac{2}{1 - \frac{\lambda_{f}}{\lambda_{r}}} \left(\frac{1}{1 - \frac{\lambda_{f}}{\lambda_{r}}} ln\left(\frac{\lambda_{s}}{\lambda_{f}}\right) - 1\right) + \frac{\lambda_{r}}{\lambda_{f}}\right) \tag{8}$$

where φ is the fractional porosity of the powder bed, λ_f is the thermal conductivity of the fluid surrounding

the powder particles (argon gas in this study) and λ_r is the thermal conductivity of the powder layer due to radiation, described by Eq. 9:

$$k_r = 4F\sigma T^3 x_r \tag{9}$$

where x_r is the average powder particle size and F = 1/3 is the view factor.

Additionally, the rule of mixtures (Alexopoulou et al. 2022) in Eq. 10 was used to predict the specific heat capacity, $C_{p,p}$ and the density of the powder bed, ρ_p .

$$C_{p,p} = \varphi C_{P,f} + (1 - \varphi) C_{P,s}$$
 (10a)

$$\rho_p = \varphi \rho_f + (1 - \varphi) \rho_s \tag{10b}$$

where $C_{p,f}$ and ρ_f are the specific heat capacity and the density of argon gas respectively.

To include radiation effects, the emissivity of the powder bed, ε_p , is required. This was predicted from the emissivity of the bulk solid phase, ε_s (Sih & Barlow 2004) and is expressed as follows:

$$\varepsilon_p = A_H \varepsilon_H + (1 - A_H) \varepsilon_s \tag{11}$$

where ε_H is the emissivity of cavities and A_H is the area fraction of the surface covered by radiating cavities, which takes the following form:



Table 2 Thermal properties for soda lime silica glass in bulk solid and powder state

Temperatur $T(^{\circ}C)$	Effective thermal conductivity for glass powder (SDV = 0) λ_{eff} (W/mK)	Thermal conductivity for bulk glass (SDV = 1) λ_s (W/mK)	Specific heat for bulk solid glass $C_{p,s}$ (J/kgK)	Specific heat for glass powder $C_{p,p}$ (J/kgK)
20	0.031	1.000	1014.20	821.16
300	0.096	1.232	1122.20	890.84
500	0.134	1.404	1202.20	942.66
700	0.164	1.576	1437.55	962.08
800	0.181	1.661	1438.20	1085.37
900	0.195	1.747	1438.85	1087.61
1000	0.209	1.833	1439.50	1089.78
1100	0.223	1.919	1440.15	1091.84
1200	0.237	2.005	1440.80	1093.79
1500	0.275	2.262	1442.75	1095.58
2000	0.332	2.691	1446.00	1097.19

Table 3 Relevant material properties used in the FEA model

Property	Variable	Value	Comments/Reference
Transition temperature	T _g (°C)	575	DSC data (Datsiou et al. 2019, 2021)
Melting temperature	$T_{\rm m}$ (°C)	1280	DSC data (Datsiou et al. 2019, 2021)
Laser absorption coefficient	H	0.27	(Datsiou et al. 2019)
Solid emissivity	$\varepsilon_{ m s}$	0.85	(Rubin 1985)
Powder bed emissivity	$arepsilon_p$	0.888	(Sih & Barlow 2004)
Average powder particle size	$x_{\rm r}$ (µm)	44	(Datsiou et al. 2019, 2021)
Powder porosity	φ	0.4	packing density of 0.6
Alumina substrate thermal conductivity (250 °C / 500 °C)	$\lambda_a(W/Mk)$	15.141 / 9.725	(Auerkari 1996)
Fused silica substrate thermal conductivity (250 °C)	$\lambda_{fs}(W/Mk)$	1.529	(Wray & Connolly 1959)

$$A_{\rm H} = \frac{0.908\varphi^2}{1.908\varphi^2 - 2\varphi + 1} \tag{12}$$

which depend on the selected glass feedstock composition.

$$\varepsilon_{\rm H} = \frac{\varepsilon_s \left(2 + 3.082 \left(\frac{1 - \varphi}{\varphi}\right)^2\right)}{\varepsilon_s \left(1 + 3.082 \left(\frac{1 - \varphi}{\varphi}\right)^2\right) + 1}$$
(13)

Based on the above, the thermal properties used in the FEA for bulk solid and powder soda lime silica glass are summarised in Table 2 as a function of temperature while other relevant material properties are available in Table 3. These include the glass melting and transition temperature as well as the laser absorption coefficient

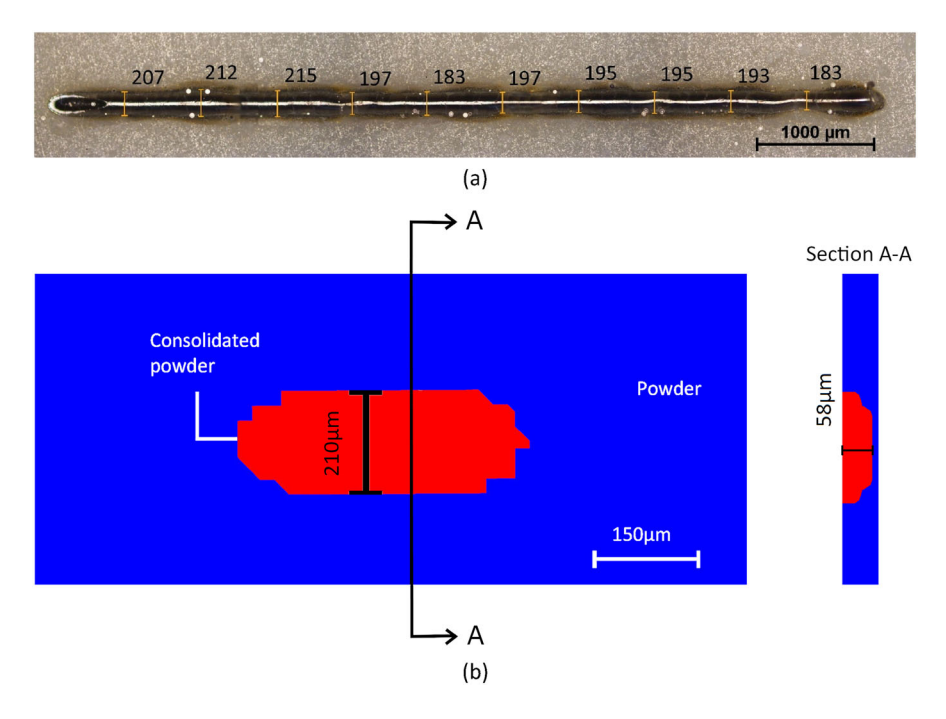
3 Results and discussion

3.1 FEA validation

Firstly, the FEA results were experimentally validated. While temperature output was not directly available, the width of the scan track was utilized to assess the accuracy of the FEA model. The experimental investigation involved a commercial benchtop LPBF system (ReaLizer GmbH SLM-50, Germany) to process the feedstock material, SLSG44 (Datsiou et al. 2021). The



Fig. 5 Single scan track illustrating the consolidated glass achieved through: a experimental testing and; b FEA



selected material provides a good match to the properties used in the FEA model of this study, although some discrepancies may be present in thermal conductivity and specific heat capacity that were derived from analytical approaches (Sect. 2.2). The feedstock material was deposited in a single layer of uniform thickness on a heated alumina substrate. A single linear scan track was undertaken with the following parameters: laser power of 75 W, scan speed of 26 mm/s, layer thickness of 0.07 mm, scan track length of 7 mm, laser focus position 9.55 mm (which corresponds to a spot size of 60 µm) and substrate temperature of 250 °C. The width of the consolidated glass powder was subsequently quantified with optical microscopy (Fig. 5a). Ten readings were obtained at equal intervals (away from the two ends) indicating an average width of 198 µm.

A FEA model replicating the parameters of the experimental test was developed. The only difference was selecting a scan track length of 0.5 mm, to minimise computational cost. The solution-dependent state variable (SDV), integrated into the USDFLF user subroutine, was used to determine the scan track width. The model predicted a width of consolidated glass (SDV = 1) of 210 μ m, ignoring the end regions of the track (Fig. 5b). This shows good agreement with experimental results with a difference of 6%.

3.2 Thermal behaviour and powder consolidation

Figure 6 illustrates the top view of a typical temperature contour for a single layer scan track, obtained using a laser power of P = 75 W and a scan speed of v =26 mm/s at a time of t = 0.01832 s. It is evident that the temperature exceeds the transition temperature of glass $(T_g = 575 \, ^{\circ}\text{C})$ and therefore powder consolidation was achieved. The consolidation region is marked with a thick black line that matches the 575 °C isotherm while the significantly smaller melt pool region, exceeding 1280 °C, is also marked. The contour isotherms on the forward part of the consolidation region are notably condensed compared to the rear part. This is attributed to the lower thermal conductivity of the powder that surrounds the forward part of the consolidation region compared to the already consolidated material at the rear, which dissipates heat at a faster rate. Moreover, it is worth noting that the 3D geometry of the consolidation region evolved with time and increased in size (Fig. 7). At the onset of laser processing, an almost hemispherical shape (e.g. t = 0.0005 s) was apparent, however, this soon transitioned into a "comet tail" geometry, a shape that agrees with common observations of melt pool during LPBF of metals, for instance in Fu & Guo, (2014).

The consolidated powder exhibited a depth of $58 \mu m$ while the width measured $210 \mu m$ (Fig. 5b) indicating



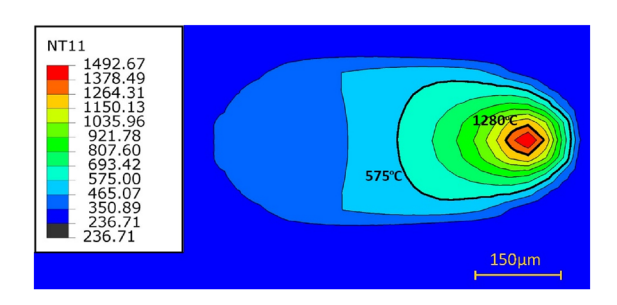


Fig. 6 Top view of temperature contours for single scan track (t = 0.01832 s)

a significant difference of 72%. This observation is in line with findings in B. Li et al., (2023) for Inconel 625 where the consolidated width exceeded the consolidated depth. However, in this case it also indicates that the laser failed to effectively consolidate the entire powder layer thickness ($t_1 = 70 \,\mu\text{m}$), which is essential in LPBF. However, "necking" of powder particles (i.e. gradual softening of powder particles and merging with one another and the substrate) was expected to occur and some degree of adhesion to the substrate to be achieved.

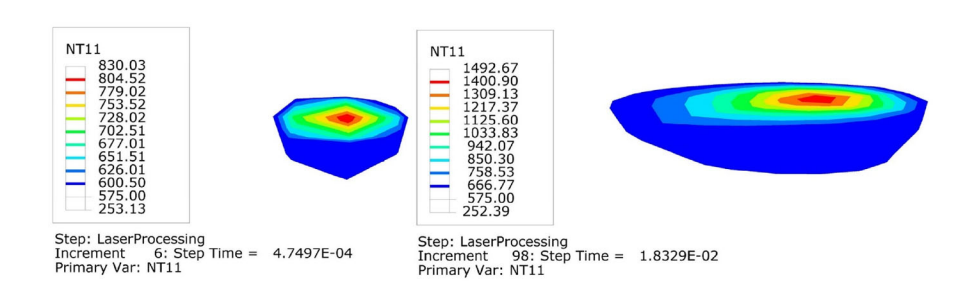
3.3 Impact of set-up and processing parameters on scan tracks

This section discusses the impact of set-up and processing parameters, including the choice of substrate and substrate temperature $T_{\rm sub}$, laser power P, scan speed v, energy density ED (Eq. 14) and hatch spacing h.

$$ED = \frac{P}{vt_l} \left(J/mm^2 \right) \tag{14}$$

Substrate temperature As discussed previously, powder consolidation was not achieved through the entire layer depth for an energy density of $ED = 41.21 \text{ J/mm}^2$ (P = 75 W, v = 26 mm/, $t_1 = 0.07 \text{ mm}$), and a substrate temperature of $T_{\text{sub}} = 250 \,^{\circ}\text{C}$ (Fig. 5b).

Fig. 7 Consolidation region evolution: hemispherical at t = 0.0005 s (left) and; "comet tail" geometry at t = 0.0183 s (right)



The same outcome was observed for scan tracks with higher energy density, confirmed up to a value of $ED \leq 108$ J/mm². This can be attributed to the significantly higher thermal conductivity of the alumina substrate ($\lambda_a = 15.1$ W/mK) compared to glass ($\lambda_s = 1.19$ W/mK and $\lambda_{\rm eff} = 0.096$ W/mK for bulk solid and powder states respectively) at 250 °C. A high rate of heat dissipation by conduction therefore occurred at the interface of the glass powder with the substrate. This prevented the development of temperatures exceeding the transition temperature of glass which is essential for powder consolidation.

However, it was found that by raising the substrate temperature to $T_{\rm sub} = 500$ °C, i.e. just below the transition temperature of glass, the entire powder layer can be consolidated (Fig. 8a). This led to a 21% increase in consolidation depth compared to a substrate temperature of $T_{\rm sub} = 250$ °C, while a 57% increase was noted for the consolidation width. Raising the substrate temperature did not affect the maximum temperature developed at the top surface of the glass powder bed during laser irradiation. It is also worth noting that powder consolidation at the lower surface did not occur simultaneously with the top surface, but lagged behind the passage of the laser source by a few ms (Fig. 8b).

Overall, raising the substrate temperature presents a twofold advantage, as not only does it increase the consolidation depth to 70 μ m, but it also reduces temperature gradients in the zone of laser treatment within the built parts during LPBF. The latter is expected to limit the development of residual stresses and consequently cracking in the built parts, as shown for zirconia ceramics in Q. Liu et al., (2015). Experimental evidence also suggested that raising the substrate temperature to 500 °C softens the glass powder particles before laser irradiation, limiting the required energy density and resulting in fully molten, transparent / "glassy" components (Spirrett 2021).



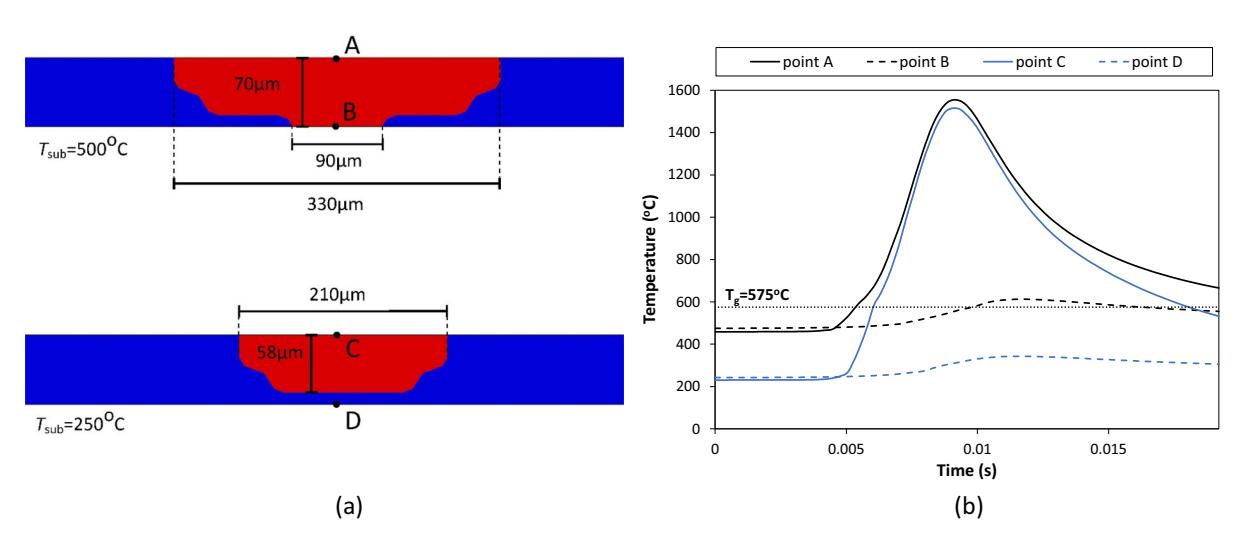


Fig. 8 a Powder consolidation (red) across the midpoint of the powder bed for substrate temperature of 250 °C and 500 °C and; b Temperature output at powder bed top and lower surfaces at points A-B for $T_{\text{sub}} = 500 \,^{\circ}\text{C}$ and B-C for $T_{\text{sub}} = 250 \,^{\circ}\text{C}$

Substrate material Substrates in LPBF are typically chosen to match the powder feedstock to ensure thermal compatibility and good adhesion. In this study, alumina substrates were selected due to their superior thermal shock resistance, as soda lime silica glass substrates were previously found to crack (Datsiou et al. 2021). However, a substrate simultaneously ensuring thermal shock resistance and compatible thermal properties (thermal conductivity and coefficient of thermal expansion) to soda lime silica glass, could be beneficial in improving the consolidation depth.

Fused silica substrates with a thermal conductivity of $\lambda_{fs} = 1.53$ W/mK at 250 °C were identified as a potential candidate in this study. Indeed, results for single scan tracks (P = 75 W and v = 26 mm/s) show that consolidation was successfully achieved through the entire powder layer at a substrate temperature of 250 °C (Fig. 9a). It was found that the choice of substrate did not affect the surface temperature development but only reduced the heat transfer by conduction at the interface with the substrate leading to the development of temperatures exceeding the transition temperature of glass (Fig. 9b). However, experimental validation is required to verify that fused silica substrates provide good adhesion with the feedstock material and that they will not exhibit cracking during the process.

Laser power The impact of laser power for a range of 20 W $\leq P \leq$ 120 W and a scan speed of 30 mm/s

was investigated for scan tracks on alumina substrates with a temperature of $T_{\rm sub} = 250$ °C to replicate the experimental set-up used in Datsiou et al., (2021).

As expected, the maximum temperature at the top glass surface increased with increasing laser power, with a linear trend (Fig. 10a). The transition temperature of glass ($T_g = 575$ °C) was exceeded in all scenarios while the melting temperature ($T_{\rm m} = 1280\,^{\circ}{\rm C}$) was exceeded for laser powers greater than 60 W. Previous experimental observations indicated that effective consolidation, resulting in well-defined walls of uniform width, was reliably achieved for laser powers exceeding 55 W at a scan speed of 30 mm/s (Datsiou et al. 2021). This reveals that high temperatures equal to or greater than the melting temperature are essential for achieving effective consolidation. While powder consolidation can occur at lower temperatures, it comes at the cost of compromising the quality of the produced parts.

The consolidation width was found to increase with laser power (Fig. 10b). Uniform widths were only noted through the thickness for laser powers of 40 W and 80 W. The remaining scenarios exhibited a wider top that progressively narrowed with increasing depth (Fig. 10c), which can compromise dimensional accuracy. It is also worth noting that the maximum consolidation depth remained constant regardless of the laser



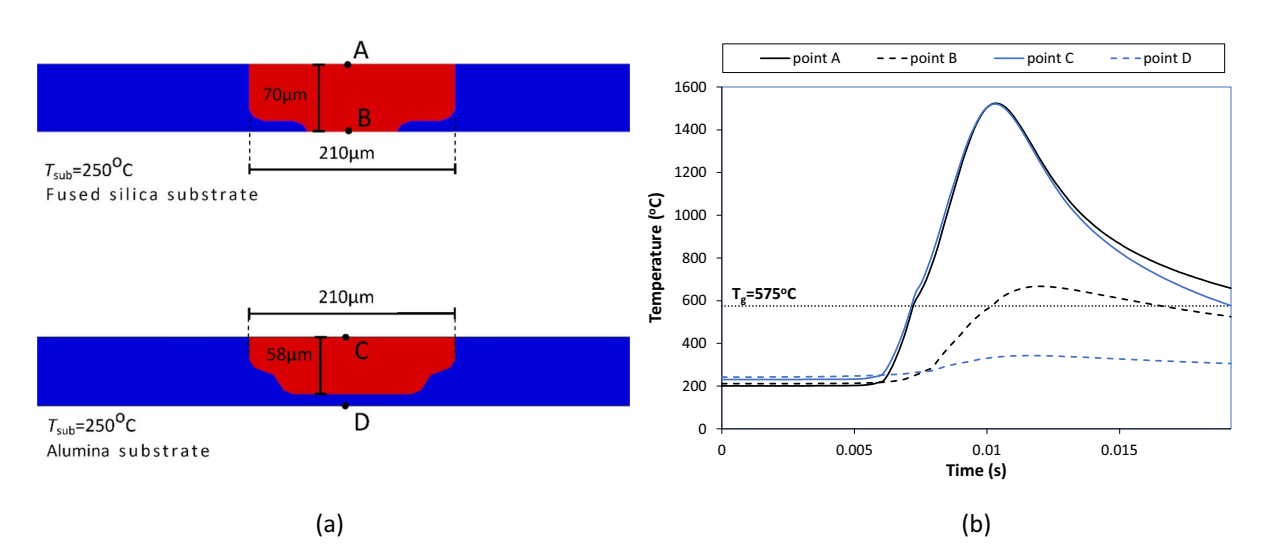


Fig. 9 a Powder consolidation (red) across the midpoint of the powder bed for alumina and fused silica substrates and; b Temperature output at powder bed top and lower surfaces at points A-B for fused silica and B-C for alumina substrates

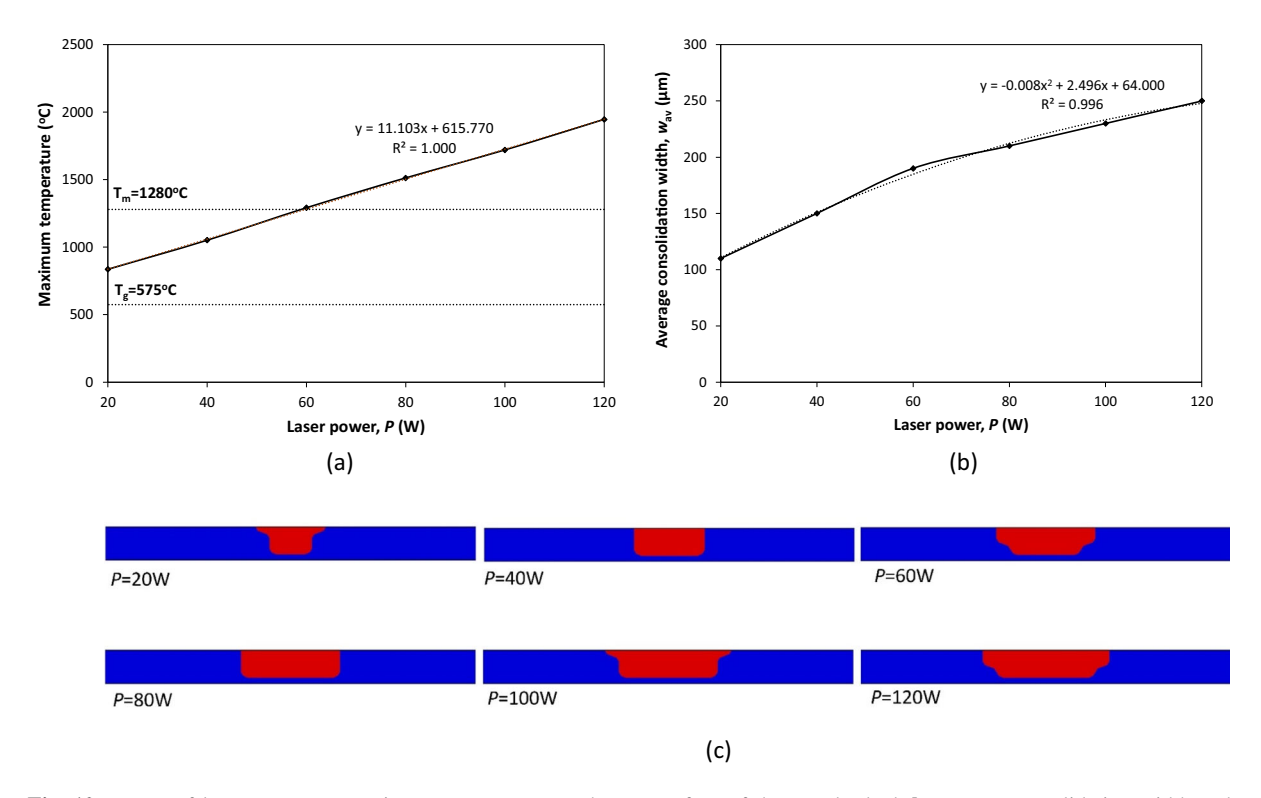


Fig. 10 Impact of laser power: a Maximum temperature at the top surface of the powder bed; b average consolidation width and; c powder consolidation (red) geometry for varying laser power



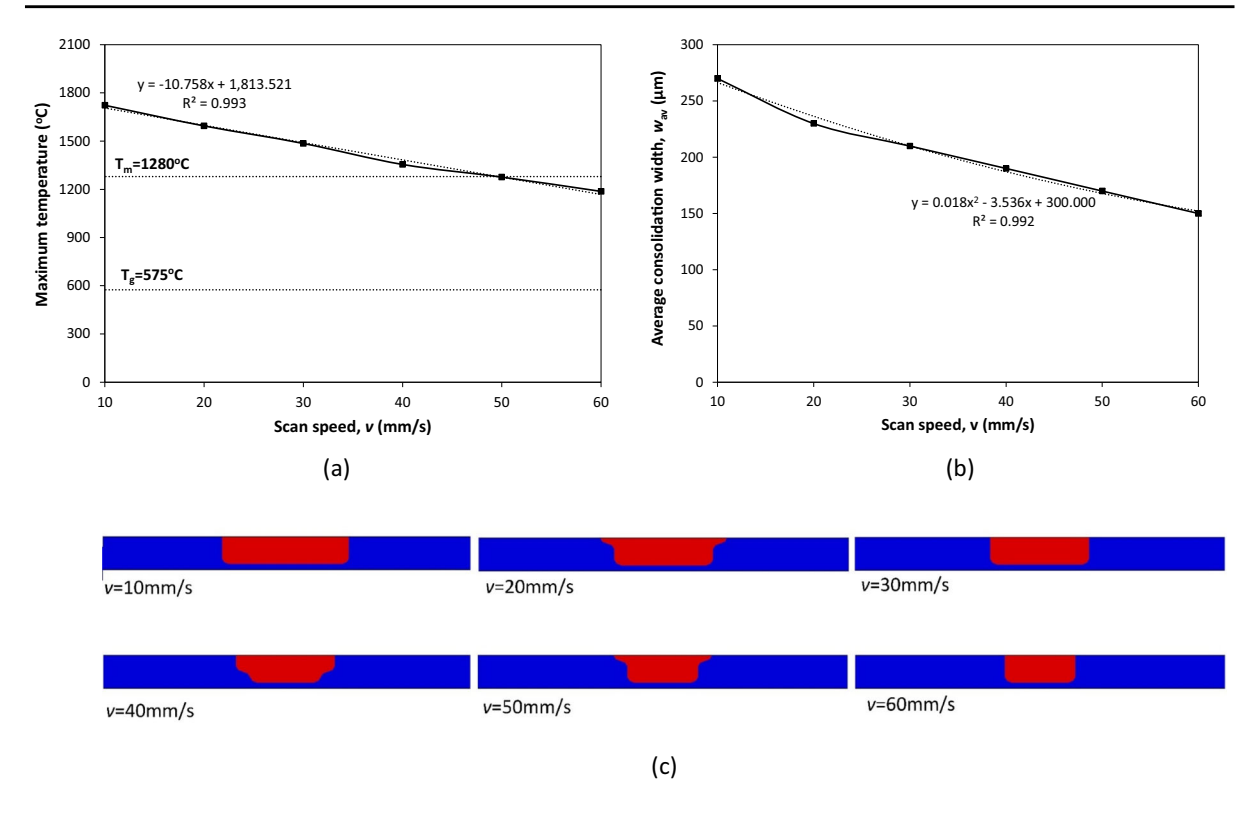


Fig. 11 Impact of scan speed: a Maximum temperature at the top surface of the powder bed; b average consolidation width and; c powder consolidation (red) geometry for varying scan speed

power employed, which can be attributed to high conductive heat transfer at the interface with the alumina substrate.

Scan speed Scan tracks with a scan speed ranging between $10 \le v \le 60$ mm/s at a laser power of P = 75 W are investigated in this section on an alumina substrate with $T_{\rm sub} = 250$ °C.

The scan speed was found to be inversely proportional to the maximum temperature at the top surface of the powder bed (Fig. 11a). The maximum temperature exceeded the transition temperature of glass in all scenarios, while the melting temperature was surpassed for scan speeds equal to or lower than 50 mm/s. This is in line with experimental observations that scan speeds exceeding 44 mm/s resulted in poor or no powder consolidation (Datsiou et al. 2021), highlighting again the significance of achieving high temperatures, close to the melting temperature of glass during thermal processing of glass powders. The average consolidation width reduced with increasing scan speed (Fig. 11b). Uniform through-the-thickness widths were noted for

scan speeds of 10, 30 and 60 mm/s while the remaining scenarios exhibited a wider top surface (Fig. 11c).

Energy density Four FEA models of scan tracks were undertaken on an alumina substrate with $T_{\rm sub} = 250\,^{\circ}{\rm C}$ featuring energy densities of $ED = 50\,{\rm J/mm^2}$ with the following parameter combinations: Scan track A: $P = 50\,{\rm W}$ and $v = 14.3\,{\rm mm/s}$, Scan track B: $P = 75\,{\rm W}$ and $v = 21.4\,{\rm mm/s}$, Scan track C: $P = 100\,{\rm W}$ and $v = 28.6\,{\rm mm/s}$ and Scan track D: $P = 125\,{\rm W}$ and $v = 35.7\,{\rm mm/s}$.

It was found that the maximum surface temperature exceeded both transition and melting temperature of glass resulting in powder consolidation for all scan tracks (Fig. 12a). However, despite maintaining a constant energy density, the achieved consolidation geometry was not consistent (Fig. 12b). Scan tracks A and B exhibited uniform consolidation widths of 210 μm whilst scan tracks C and D displayed a wider top of 270 μm , although they also shared the 210 μm width in the lower part of the consolidated layer (Fig. 12b). It was found that the simultaneous increase of laser power



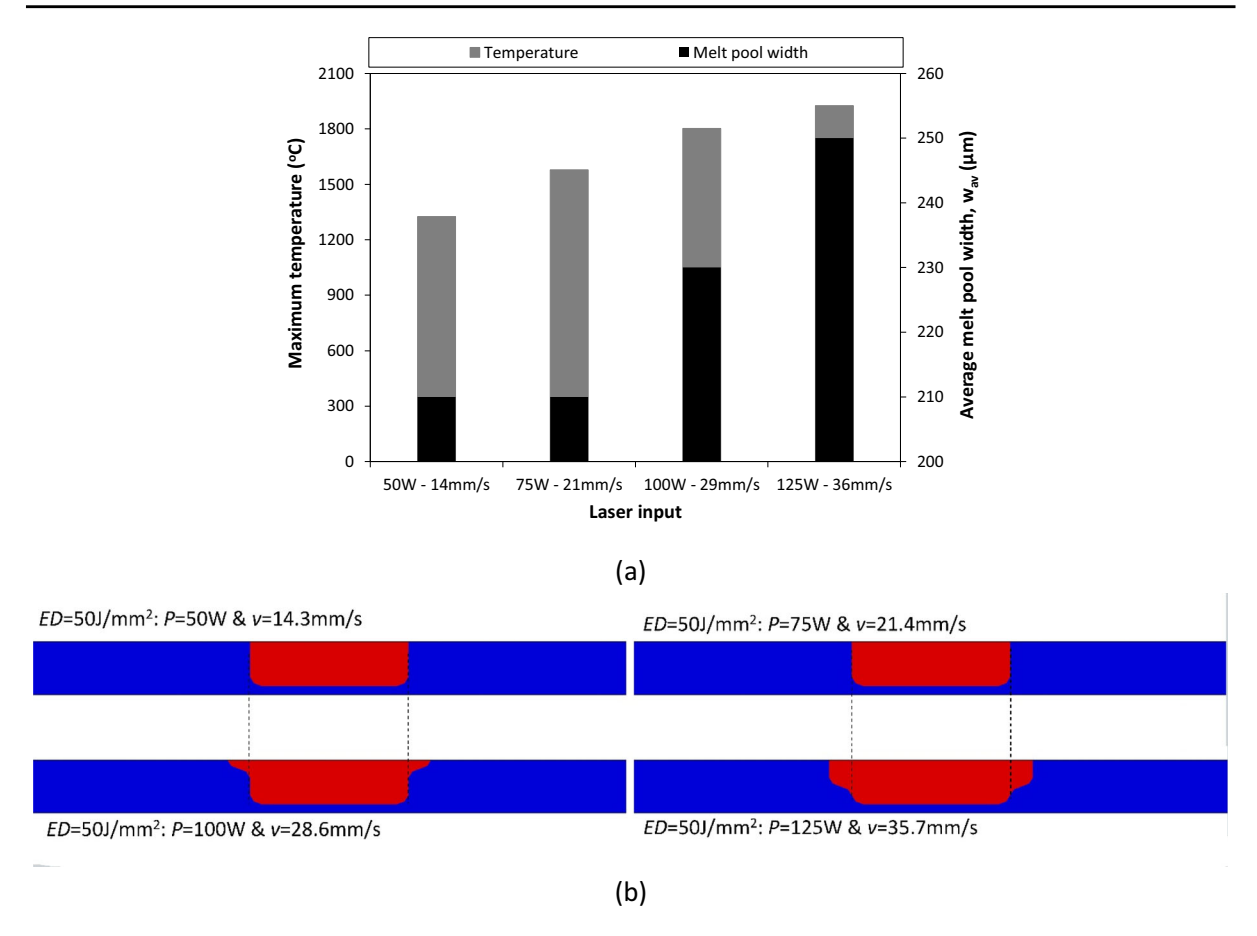


Fig. 12 Scan tracks of the same energy density but varying laser power and scan speed: a Maximum temperature at the top surface of the powder bed and average consolidation width and; b powder consolidation (red) geometry

and scan speed resulted in a rise in maximum temperature (Fig. 12a). These temperatures expanded the heat affected zone at the surface of the powder bed for scan tracks C and D leading to a wider consolidation top, but without any significant difference in depth.

Hatch spacing Three consecutive unidirectional linear scan tracks, placed next to one another, were modelled in this section to identify the impact of hatch spacing between adjacent laser trajectories. A FEA model with laser power of P=80 W, scan speed of v=30 mm/, layer thickness of $t_1=0.07$ mm and substrate temperature of $T_{\rm sub}=250$ °C was employed for hatch spacings of 90 μm (HS90), 150 μm (HS150), 210 μm (HS210) and 270 μm (HS270).

The consolidation width for a single scan track under the specified processing parameters was $w_{c,st} = 210 \,\mu m$ (Fig. 10b). As expected, hatch spacings exceeding $w_{c,st}$ did not yield continuous consolidation, instead resulted

in distinct scan tracks (Fig. 13). Continuous consolidation on the top surface of the powder bed could be achieved for hatch spacings equal to or lower than $h \le w_{\rm c,st}$ while the total consolidation width for all 3 unidirectional scan tracks increased with increasing hatch spacing (from 390 to 630 μ m for hatch spacings of 90 to 210 μ m respectively). A hatch spacing equal to $w_{\rm c,st}$, however, failed to create a uniform consolidation depth which was instead apparent for $h < w_{\rm c,st}$ (90 and 150 μ m in this case). The above suggest that hatch spacings smaller than the individual scan track width are preferrable. This will ensure a uniform consolidation depth and prevent the encapsulation of pockets of unfused powder particles within the built parts that compromise their quality.

Irrespective of the selected hatch spacing, the maximum temperature in all scan tracks was found to be very similar (Fig. 14). However, for hatch spacing of



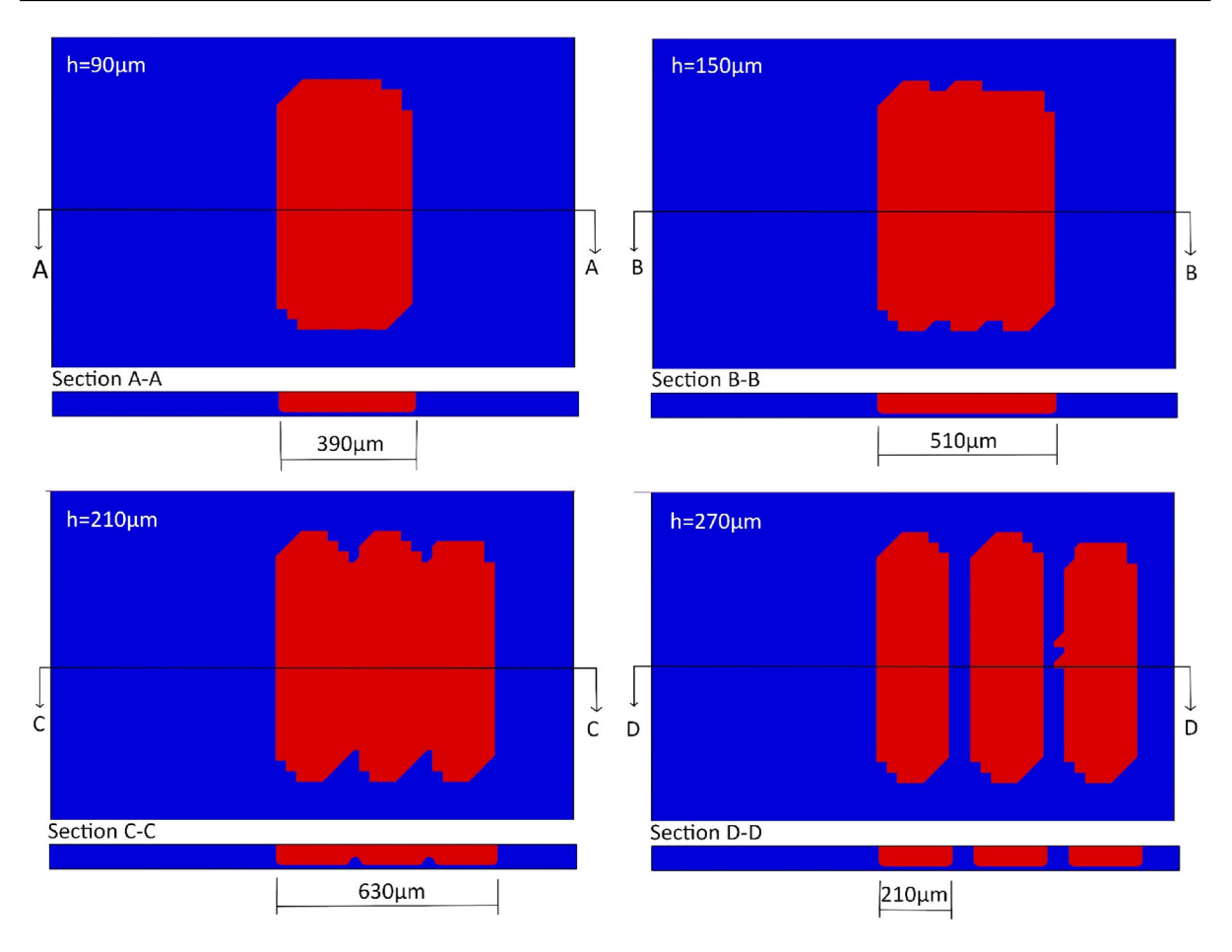


Fig. 13 Top view and cross section of powder consolidation (red) for three adjacent unidirectional scan tracks at hatch spacings of $h = 90 \mu \text{m}$ (top left), 150 μm (top right), 210 μm (bottom left) and 270 μm (bottom right)

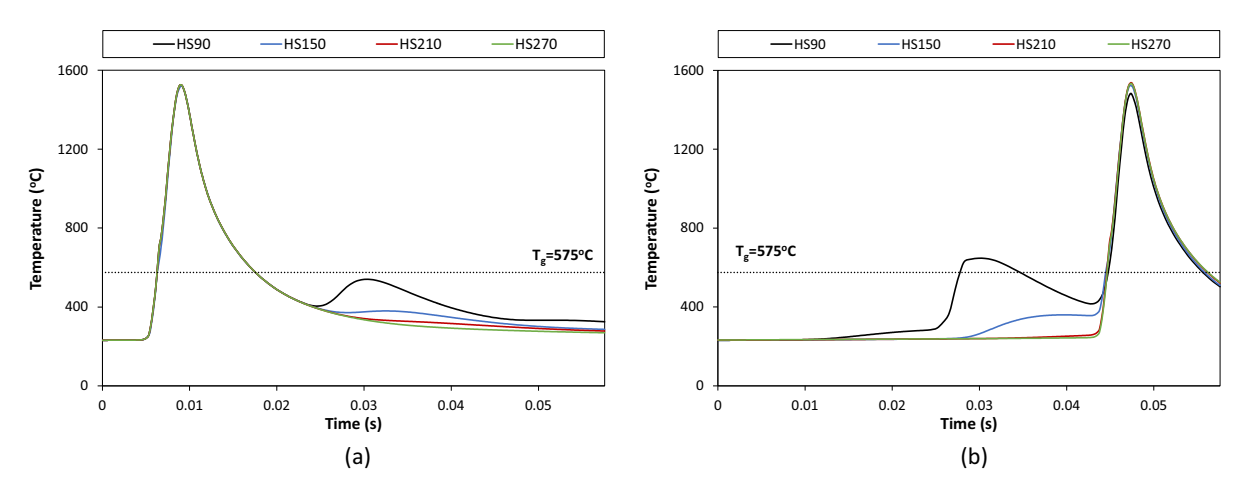


Fig. 14 Temperature output for the midpoint of the: a first and; b second scan track during laser processing



 $90~\mu m$, it was noted that softening / fusing of powder particles could occur twice for adjacent scan tracks as the temperature at the midpoint of the second scan track exceeded the glass transition temperature both during the first scan track and during the second scan track i.e. when the laser source passes from that point. This was a direct result of the denser hatch spacing. Although reprocessing of powder particles could improve built part quality, care should be taken to avoid excessive energy density input that could result in spherical features and deviation from flatness at the top surface (Datsiou et al. 2021), typically referred to as "balling", which warrants further investigation.

4 Conclusions

This study developed a transient heat transfer finite element analysis model to shed light on the laser powder bed fusion process for soda lime silica glass. The thermal response of the process was captured while the impact of laser processing and substrate parameters were investigated. Temperature dependent thermophysical material properties were used as input for both glass powder and bulk solid states. Fortran coding in user subroutines was undertaken to simulate the moving laser heat source, conversion from powder feedstock to bulk solid glass and convection and radiation effects. The model was validated against available experimental data on single scan tracks. Salient conclusions drawn from this work are summarised as follows:

- The evolution of the glass consolidation region exhibited an initial hemispherical shape at the beginning of laser irradiation, quickly transitioning into a distinctive "comet tail" geometry, mirroring similar phenomena observed in laser powder bed fusion of metals.
- Alumina substrates at usual preheating temperatures
 (~ 250 °C) prevented powder consolidation through
 the entire powder layer. High heat dissipation by
 conduction occurs at the interface of the powder
 feedstock with the substrate, due to the significantly
 higher thermal conductivity of alumina compared
 to glass. Two distinct mitigations strategies have
 been identified in this study to improve consolida tion depth namely, to increase the substrate preheat ing temperature to 500 °C (just below the transition
 temperature of glass) or to replace alumina with a

- thermal shock resistant material that is also thermally compatible with glass such as fused silica.
- Increasing laser power was observed to lead to increased maximum surface temperature and consolidation width whereas the inverse effect was noted for increasing scan speeds. Interestingly, surface temperatures and consolidation geometries were found to vary among scan tracks of equal energy density but different laser power and scan speed. This highlights the need for further investigation to understand the underlying factors contributing to this phenomenon.
- Although some degree of powder consolidation can be achieved for temperatures exceeding the transition temperature of glass, the combination of numerical results of this study with previous experimental observations revealed that effective powder consolidation, resulting in well-defined features, can be achieved when operating at temperatures within the proximity of the glass melting point.
- Uniform consolidation width and depth in a unidirectional scan strategy were effectively achieved when the hatch spacing was set below the corresponding single scan track width. This configuration ensured continuous and seamless consolidation across the laser processed layer.

These findings offer useful insights for the laser powder bed fusion of glass and should be considered for future practical applications. However, to comprehensively address the limitations of LPBF, further numerical investigation is necessary. A coupled thermomechanical analysis is recommended to understand the development of residual stresses and to capture temperature dependent volumetric changes in the glass. This will provide the foundation for developing mitigation strategies aimed at minimizing residual stresses and associated cracking, which will ultimately contribute to the improvement of strength and the overall quality of the built glass parts.

Data availability Data generated during the current study are available from the corresponding author on reasonable request.

Open Access This article is licensed under a Creative Commons Attribution 4.0 International License, which permits use, sharing, adaptation, distribution and reproduction in any medium or format, as long as you give appropriate credit to the original author(s) and the source, provide a link to the Creative Commons licence, and indicate if changes were made. The images or other third party material in this article are included in the



article's Creative Commons licence, unless indicated otherwise in a credit line to the material. If material is not included in the article's Creative Commons licence and your intended use is not permitted by statutory regulation or exceeds the permitted use, you will need to obtain permission directly from the copyright holder. To view a copy of this licence, visit http://creativecommons.org/licenses/by/4.0/.

References

- Abaqus 2023 Documentation. (2023). Analysis User's Manual. Dassault Systèmes Simulia Corp.
- Alexopoulou, V.E., Papazoglou, E.L., Karmiris-Obratański, P., Markopoulos, A.P.: 3D finite element modeling of selective laser melting for conduction, transition and keyhole modes. J. Manuf. Process. 75(January), 877–894 (2022). https:// doi.org/10.1016/j.jmapro.2022.01.054
- Auerkari, P. (1996). Mechanical and physical properties of engineering alumina ceramics. Technical Research Centre of Finland.
- Batalha, R.L., Batalha, W.C., Deng, L., Gustmann, T., Pauly, S., Kiminami, C.S., Gargarella, P.: Processing a biocompatible Ti-35Nb-7Zr-5Ta alloy by selective laser melting. J. Mater. Res. 35(9), 1143–1153 (2020). https://doi.org/10.1557/jmr. 2020.90
- Carré, H., Daudeville, L.: Load-bearing capacity of tempered structural glass. J. Eng. Mech. 125(8), 914–921 (1999). https://doi.org/10.1061/(asce)0733-9399(1999)125:8(914)
- Dai, K., Shaw, L.: Thermal and mechanical finite element modeling of laser forming from metal and ceramic powders. Acta Mater. 52(1), 69–80 (2004). https://doi.org/10.1016/j.actamat.2003.08.028
- Datsiou, K.C., Saleh, E., Spirrett, F., Goodridge, R., Ashcroft, I., Eustice, D.: Additive manufacturing of glass with laser powder bed fusion. J. Am. Ceram. Soc. (2019). https://doi.org/10.1111/jace.16440
- Datsiou, K.C., Spirrett, F., Ashcroft, I., Magallanes, M., Christie, S., Goodridge, R.: Laser powder bed fusion of soda lime silica glass: Optimisation of processing parameters and evaluation of part properties. Addit. Manuf.. Manuf. 39, 101880 (2021). https://doi.org/10.1016/j.addma.2021.101880
- Fateri, M., Gebhardt, A.: Selective Laser Melting of soda-lime glass powder. Int. J. Appl. Ceram. Technol. 12(1), 53–61 (2015). https://doi.org/10.1111/ijac.12338
- Fu, C.H., Guo, Y.B.: Three-dimensional temperature gradient mechanism in selective laser melting of Ti-6Al-4V. J. Manuf. Sci. E. T. ASME 136(6), 1–8 (2014). https://doi.org/10.1115/1.4028539
- Grabe, T., Lammers, M., Wang, S., Wang, X., Rettschlag, K., Sleiman, K., Barroi, A., Biermann, T., Ziebehl, A., Röttger, J., Ley, P.-P., Wolf, A., Jaeschke, P., Hermsdorf, J., Kaierle, S., Ahlers, H., Lachmayer, R.: Additive anufacturing of fused silica using coaxial laser glass deposition: experiment, simulation and discussion. Laser 3D Manuf. 11677, 32 (2021). https://doi.org/10.1117/12.2577205
- Gusarov, A.V., Smurov, I.: Modeling the interaction of laser radiation with powder bed at selective laser melting. Phys. Procedia 5(2), 381–394 (2010). https://doi.org/10.1016/j.phpro.2010.08.065

- Inamura, C., Stern, M., Lizardo, D., Houk, P., Oxman, N.: Additive manufacturing of transparent glass structures. 3D Print. Addit. Manuf. 5(4), 269–283 (2018). https://doi.org/ 10.1089/3dp.2018.0157
- Kamyabi, M., Sotudeh-Gharebagh, R., Zarghami, R., Saleh, K.: Principles of viscous sintering in amorphous powders: A critical review. Chem. Eng. Res. Des. 125, 328–347 (2017). https://doi.org/10.1016/j.cherd.2017.06.009
- Klein, J. (2015). Additive Manufacturing of Optically Transparent Glass [Master's thesis, Massachusetts Institute of Technology (MIT)]. https://doi.org/10.1201/b19360
- Kolossov, S., Boillat, E., Glardon, R., Fischer, P., Locher, M.: 3D FE simulation for temperature evolution in the selective laser sintering process. Int. J. Mach. Tools Manuf 44(2–3), 117–123 (2004). https://doi.org/10.1016/ j.ijmachtools.2003.10.019
- Kotz, F., Arnold, K., Bauer, W., Schild, D., Keller, N., Sachsenheimer, K., Nargang, T.M., Richter, C., Helmer, D., Rapp, B.E.: Three-dimensional printing of transparent fused silica glass. Nature 544(7650), 337–339 (2017). https://doi.org/10.1038/nature22061
- Li, Y., Gu, D.: Parametric analysis of thermal behavior during selective laser melting additive manufacturing of aluminum alloy powder. Mater. Des. 63, 856–867 (2014). https://doi. org/10.1016/j.matdes.2014.07.006
- Li, J., Wei, Z., Yang, L., Zhou, B., Wu, Y., Chen, S.G., Sun, Z.: Finite element analysis of thermal behavior and experimental investigation of Ti6Al4V in selective laser melting. Optik 207, 163760 (2020). https://doi.org/10.1016/j.ijleo. 2019.163760
- Li, B., Du, J., Sun, Y., Zhang, S., Zhang, Q.: On the importance of heat source model determination for numerical modeling of selective laser melting of IN625. Opt. Laser Technol. 158(PA), 108806 (2023). https://doi.org/10.1016/j.optlastec.2022.108806
- Liu, Q., Danlos, Y., Song, B., Zhang, B., Yin, S., Liao, H.: Effect of high-temperature preheating on the selective laser melting of yttria-stabilized zirconia ceramic. J. Mater. Process. Technol. 222, 61–74 (2015). https://doi.org/10.1016/ j.jmatprotec.2015.02.036
- Liu, C., Qian, B., Ni, R., Liu, X., Qiu, J.: 3D printing of multicolor luminescent glass. RSC Adv. 8(55), 31564–31567 (2018). https://doi.org/10.1039/c8ra06706f
- Liu, B. (2013). Further Process Understanding and Prediction on Selective Laser Melting of Stainless Steel 316L. In *PhD* thesis. Loughborough University.
- Nguyen, D.T., Meyers, C., Yee, T.D., Dudukovic, N.A., Destino, J.F., Zhu, C., Duoss, E.B., Baumann, T.F., Suratwala, T., Smay, J.E., Dylla-Spears, R.: 3D-printed transparent glass. Adv. Mater. 29(26), 1–5 (2017). https://doi.org/10.1002/ adma.201701181
- Papazoglou, E.L., Karkalos, N.E., Karmiris-Obratański, P., Markopoulos, A.P.: On the modeling and simulation of SLM and SLS for metal and polymer powders: a review. Arch. Comput. Methods Eng. (2022). https://doi.org/10. 1007/s11831-021-09601-x
- Parry, L., Ashcroft, I.A., Wildman, R.D.: Understanding the effect of laser scan strategy on residual stress in selective laser melting through thermo-mechanical simulation. Addit. Manuf. 12, 1–15 (2016). https://doi.org/10.1016/j. addma.2016.05.014



- Roberts, I.A., Wang, C.J., Esterlein, R., Stanford, M., Mynors, D.J.: A three-dimensional finite element analysis of the temperature field during laser melting of metal powders in additive layer manufacturing. Int. J. Mach. Tools Manuf **49**(12–13), 916–923 (2009). https://doi.org/10.1016/j.ijmachtools.2009.07.004
- Rubin, M.: Optical properties of soda lime silica glasses. Solar Energy Mater. **12**(3), 275–288 (1985). https://doi.org/10. 1016/0165-1633(85)90052-8
- Sih, S.S., Barlow, J.W.: Measurement and prediction of the thermal conductivity of powders at high temperatures. Solid Freeform Fabrication **321**(1), 321–329 (1992)
- Sih, S.S., Barlow, J.W.: The prediction of the emissivity and thermal conductivity of powder beds. Part. Sci. Technol. 22(4), 427–440 (2004). https://doi.org/10.1080/02726350490501682
- Spirrett, F.: Investigations into Glass Additive Manufacturing by Selective Laser Melting and Directed Energy Deposition. University of Nottingham (2021)
- Spirrett, F., Datsiou, K.C., Magallanes, M., Ashcroft, I., Goodridge, R.: Powder-fed directed energy deposition of soda lime silica glass on glass substrates. J. Am. Ceram. Soc. 106(1), 227–240 (2023). https://doi.org/10.1111/jace. 18638
- Wray, K.L., Connolly, T.J.: Thermal conductivity of clear fused silica at high temperatures. J. Appl. Phys. **30**(11), 1702–1705 (1959). https://doi.org/10.1063/1.1735040
- Wu, J., Wang, L., An, X.: Numerical analysis of residual stress evolution of AlSi10Mg manufactured by selective laser melting. Optik 137, 65–78 (2017). https://doi.org/10.1016/ j.ijleo.2017.02.060
- Xin, C., Li, Z., Hao, L., Li, Y.: A comprehensive review on additive manufacturing of glass: Recent progress and future outlook. Mater. Des. 227, 111736 (2023). https://doi.org/10.1016/j.matdes.2023.111736

Zhang, D., Zhang, P., Liu, Z., Feng, Z., Wang, C., Guo, Y.: Thermofluid field of molten pool and its effects during selective laser melting (SLM) of Inconel 718 alloy. Addit. Manuf. 21(100), 567–578 (2018). https://doi.org/10.1016/j.addma. 2018.03.031

Publisher's Note Springer Nature remains neutral with regard to jurisdictional claims in published maps and institutional affiliations

